Metallurgical factors governing water oxidation-transpassive dissolution interplay and transpassive intergranular corrosion susceptibility of non-sensitized Ni-Fe-Cr alloys

Karthikeyan Hariharan[1,2*#], Koushik Kosanam[1#], Elisabeth Kammermeier[3], Christopher H. Zenk[3], Sannakaisa Virtanen[1*]

[1]Friedrich-Alexander-Universität Erlangen-Nürnberg, Department of Materials Science & Engineering, Institute IV: Surface Science and Corrosion (LKO), Erlangen, Germany.

[2]Corrosion Metallurgy Laboratory, Department of Metallurgical Engineering and Materials Science, Indian Institute of Technology Bombay, Mumbai, India.

[3]Friedrich-Alexander-Universität Erlangen-Nürnberg, Department of Materials Science & Engineering, Institute II: Materials Science and Metals Engineering (WTM), Erlangen, Germany.

Corresponding Authors (karthik.hariharan@iitb.ac.in , sannakaisa.virtanen@fau.de)

[#]Authors contributing Equally

Abstract

This study investigates metallurgical factors influencing the interplay between oxygen evolution reaction (OER)/water oxidation and alloy dissolution as well as the intergranular corrosion (IGC) susceptibility of Ni-Cr-Fe corrosion-resistant alloys (Alloy 600, Alloy 800 and model Ni-15Cr-10Fe) in 0.1 M K_2SO_4 (pH =5) at transpassive potentials. The total anodic charge passed is fully accounted by the transpassive dissolution in Alloy 600, against only 50% accounting for dissolution in Alloy 800. In fact, Alloy 800 suffered 6 times lower dissolution than Alloy 600 under the same electrochemical conditions. In terms of localized corrosion, Alloy 600 suffers from severe IGC and grain-fallout, while Alloy 800 experiences lower IGC resisting grain-fallout. While the lower overall dissolution in Alloy 800 is explained by secondary passivation due to higher Fe content, IGC seems to be strongly influenced by special grain boundaries (GBs) and their interconnectivity. The fraction of special GBs ($\Sigma \leq 29$) and resistant triple junctions increase between Alloy 600 and Alloy 800, coinciding with decreasing IGC susceptibility. Further analysis on model Ni-15Cr-10Fe alloy under two different heat treatments revealed that the interconnectivity of special GBs had a greater influence in governing the transpassive IGC than the absolute special GB fraction, at a fixed Fe content.

Keywords

grain boundary structure; intergranular corrosion; transpassivity; nickel alloys

1. Introduction

Ni-Cr-Fe corrosion-resistant alloys (CRAs) are tuned to exhibit excellent corrosion resistance through formation of a thin, protective Cr-rich passive film [1]. However, under high anodic potentials/in highly oxidizing environments, these CRAs lose their passivity and enter the transpassive regime [2-5]. There is a renewed interest in investigating the transpassive regime due to increasing practical relevance in terms of applications such as fuel-cell bipolar plates [6-9] and nuclear waste reprocessing plants [10-12], where the operating conditions take these alloys into transpassive regime. The transpassive corrosion mechanisms are also relevant to high temperature-high pressure environments including in nuclear reactors and organic waste supercritical oxidation treatment plants. For example, Ni-Cr-Fe Alloy 600 underwent intergranular stress corrosion cracking (primary water stress corrosion cracking) during constant extension rate tests carried out at transpassive potentials but did not crack in the passive range[13]. Furthermore, intergranular corrosion of Ni-based Alloy 625 was reported to occur under conditions of supercritical water oxidation of organic wastes [14, 15].

The key issue in the transpassive regime in Cr-passivated alloys is the loss of protection from Cr-rich passive film that prevented corrosion. In the transpassive regime, Cr_2O_3 or $Cr(OH)_3$ undergoes further oxidation to form Cr (VI) species such as chromate (CrO_4^{2-}) in basic pH or dichromate ($Cr_2O_7^{2-}$) in acidic pH [16], through the following reactions as follows (Eq. (1) to Eq. (5)) [5]:

$$Cr_2O_3 + 4H_2O = Cr_2O_7^{2-} + 8H^+ + 6e^- \quad (1)$$

$$2Cr(OH)_3 + H_2O = Cr_2O_7^{2-} + 8H^+ + 6e^- \quad (2)$$

$$Cr_2O_3 + 10OH^- = 2CrO_4^{2-} + 5H_2O + 6e^- \quad (3)$$

$$Cr(OH)_3 + 5OH^- = CrO_4^{2-} + 4H_2O + 3e^- \quad (4)$$

While Cr is no longer protective under transpassive conditions, Fe could potentially curb the alloy dissolution [4, 17], through Fe-rich NiFeOOH secondary passive film. While studies show reduced total anodic currents in Fe-rich alloys, it is not clear if this is due to reduced alloy dissolution, as there are other reactions such as oxygen evolution reaction (OER) occurring

simultaneously under these conditions [18]. Therefore, we need to use complementary non-electrochemical testing methods such as *in situ* respirometry along with conventional electrochemical polarization experiments. While respirometry was initially developed to study cathodic reactions such as hydrogen evolution or oxygen reduction reaction [19-21]. Recent studies, including our own study on pure Ni has shown the applicability to tracking an anodic water oxidation reaction (i.e. OER) [18] and decouple it from dissolution and secondary passive film formation.

In addition to studying the effect of Fe alloying in determining the OER-dissolution interplay in the transpassive regime, it is essential to study factors affecting localized intergranular corrosion in the transpassive regime [22, 23], which can pose a challenge to structural integrity of the alloys. Moreover, there is substantial literature showing Alloy 600 subjected to IGC and IGSCC in variety of environments, making an important aspect to investigate further [24-26].

The transpassive IGC does not stem from chromium depletion at the vicinity of GBs, as it occurred even in case of ultra-pure (99.999%) Ni. Palumbo and Aust studied the IGC in pure Ni in the transpassive regime showed that the special coincidence-site lattice (CSL) GBs resisted IGC [23]. Therefore, increasing the fraction of these CSL GBs could make the alloys resistant to IGC in the transpassive regime. The beneficial effect of special CSL GBs to the classical form of IGC in Alloy 600 [29] and Alloy 800 [30] is well known, while there is no study exploring the role of CSL GBs on transpassive IGC in Ni-Cr-Fe alloys. Furthermore, the literature also suggests that it is not just the fraction of special CSL GBs that governs the IGC, but it is also influence by how well they are connected within the microstructure (i.e. special triple junctions), as interconnected special GBs prevent percolation [31-34].

In this work, we investigate the phenomena of transpassive IGC using two commercial single-phase austenitic Ni-Cr-Fe CRAs – Alloy 600 and Alloy 800 and a model Ni-15Cr-10Fe alloy to investigate the role of alloy chemistry (i.e. Fe contents) and microstructure (i.e. GB nature) using a combination of electrochemical polarization coupled with *in situ* respirometry with microstructural effects investigated using electron backscattered diffraction (EBSD) analysis of grain boundary character distribution (GBCD).

2. Materials and Methods

2.1 Materials – Composition and Heat treatment

Alloy 600 and Alloy 800 plates of 1 mm thickness were procured from Goodfellow, UK in solution annealed condition. The model alloy with nominal composition (wt.%) Ni-15Cr-10Fe ingot was vacuum arc melted, homogenized, and subject to cold rolling up to 50% area reduction and was subject to recrystallization at two conditions – one set was held at 850 ^{o}C for 1 h followed by water quenching, and the other set was held at 1100 ^{o}C for 30 min followed by water quenching. The actual composition of all the three alloys was measured using spark optical emission spectroscopy (OES) – Table 1.

2.2 Specimen preparation for potentiodynamic respirometry experiments

The alloy plates were cut into small square pieces (approximately 0.75 cm x 1 cm), and they were mechanically ground using 600-grit and 1200-grit SiC papers followed by polishing in a polycrystalline diamond paste of 3 μm grit size on both sides. Then, the specimen surface was rinsed with deionized water for cleaning. After the polishing, a 304L stainless steel wire (0.5 mm diameter) was spot welded to one side of the sample for establishing electrical contact during the experiment. The samples were coated with a blue laquear to control the exposed area to approximately 0.05 cm^2 to 0.1 cm^2, as well as to cover the spot-welded portion as shown in Figure 1a.

2.3 Metallographic preparation for electron backscattered diffraction analysis

Square samples cut from all the 3 alloy plates were mounted using a conductive mounting powder. The mounted samples underwent mechanical polishing up to 1200-grit SiC paper, followed by polishing in polycrystalline diamond paste of 3 μm and 1 μm grit sizes, successively. Final polishing for EBSD analysis was done with a non-crystallizing colloidal silica suspension for 24 h in a vibratory polisher. The polished samples were cleaned and sonicated in deionized water, ethanol, and again in deionized water, successively for 10 min each.

2.4 Potentiodynamic respirometry experiments

The potentiodynamic respirometry measurements were carried out using a PalmSens 4 electrochemical workstation (PalmSens BV, The Netherlands) in a three-electrode setup with Ag/AgCl (satd. KCl) electrode as reference, and platinum sheet as a counter electrode. The counter electrode was placed in a separate compartment that was connected to the working electrode chamber and ionic contact was established using a NafionTM membrane, while making sure the chambers were gas and electrolyte flow tight. The reference was also separated from the working electrode chamber. A connection was made to the working compartment through a metal bridge made of 304L stainless steel[35], to prevent chloride contamination of the electrolyte and hence preventing pitting artifact.
The working electrode compartment itself was a 10 mL glass vessel (Duran® GL25) with a port for connecting to the counter electrode compartment. The working electrode chamber was hermetically sealed and the contactless PyroScience optical O_2 sensor spots glued on to the inner surface of the chamber walls for measuring the oxygen in the electrolyte phase as well as the headspace above the electrolyte. The response time of these sensors is about 10 s as shown in the work of our collaborators using benchmark experiments on Pt using galvanostatic pulse [36]. We must note that we are scanning at a rather slow 0.5 mV/s –assuming 10 s response time, it would lead only in a potential shift of 5 mV, which is well within the error range of the reference electrodes. Therefore, the OER measurements can be considered as real-time, and can be used to indirectly infer dissolution rates.

The signals were recorded by a fiber optic O_2 meter (Firesting® PRO probe, PyroScience GmbH), the free ends of the two fiber optic cables were held in place behind the sensor spots on the outer wall (see schematic in Figure 1b) of the working electrode compartment, and data collection took place at a rate of 0.1 Hz. During the measurements, the entire setup was submerged in water using a water bath, and temperature variations during the experiment were monitored continuously using Pt100 temperature probe placed close to the outer walls of the working compartment. Further details about the calibration, working principle, response time, detection limits, and resolution of the sensor are well described in our recent work [37] and the work of our collaborators [38].

The electrochemical polarization sequence involved hold at the open circuit potential (OCP) for 1 h to attain a reasonable steady state followed by potentiodynamic polarization starting at +0 V vs. OCP up to +2 V (vs. Ag/AgCl (sat. KCl)) at a scan rate of 0.5 mV/s. During the experiment, the electrolyte was continuously stirred at 200 rpm using a magnetic stir bar. The 0.1 M K_2SO_4 electrolyte was freshly prepared before the experiment, with pH of the electrolyte adjusted to 5 just before the start of the measurement by pipetting desired quantities of sulfuric acid. The tests were repeated thrice to validate reproducibility.

After the experiments, the sample surface was imaged using optical microscope to check for intergranular attack. Furthermore, the alloy was electroplated with Ni and cut with a low speed saw. The cross-section was mounted in epoxy and polished up to 1 μm, and the cross-section was imaged with and without etching. Immersion etching ASTM Etchant No. 25 was used to etch the cross-section to clear visualize the presence of IGC, especially for Alloy 600, where grains suffered grain fall-out.

2.5 XPS analysis

XPS analysis was performed on the Alloy 600 and Alloy 800 samples following the polarization test, after removing laquear. A monochromate Al Kα X-ray source (hv = 1486.6 eV) was used with an X-ray spot size of 600 μm in diameter. The base pressure of the pump was maintained at 4X 10^{-7} torr throughout the measurement. Survey spectra were recorded with a pass energy of 187.85 eV at a step size of 0.2 eV, and high-resolution spectra of the C 1 s, O 1 s, Cr 2p, Ni 2p, and Fe 2p core levels were recorded with a pass energy of 23.5 eV and 45^{o} take off angle. To correct for the surface charging effects, the binding energy scale was calibrated by referencing the adventitious carbon C 1s peak to 284.8 eV.

2.6 Depth of attack analysis using 3D laser scanning confocal microscopy

Depth of attack for both alloys was analyzed using 3D laser scanning confocal microscopy (LEXT OLS4000) with white LED Light and 2-megapixel CCD Detector. It is equipped with Laser Imaging Mode with 405 nm Laser and Photomultiplier Detector. It has a lateral (XY) resolution of ~120 nm and minimum Z-Resolution of 10 nm. The depths of attack were estimated by measuring the height difference between the uncorroded surface in the vicinity of the GB and the

attacked GB, using the step mode of measurement. 50 attacked grain boundaries were sampled to ensure the depths of attack are statistically meaningful and representative of the material behavior. Moreover, the depth of attack measurements avoided regions where the grains had completely fallen off to exclude material loss from the non-faradaic "grain fallout" from skewing the measured depth of attack.

2.7 Data analysis for respirometric measurements

The goal of the respirometric measurement is to decouple the contributions of dissolution from that of OER. To accomplish that, the O_2 sensor readings from electrolyte phase in mg/L were converted to number of moles of oxygen evolved by multiplying the electrolyte volume. Similarly, oxygen partial pressure changes in the headspace are converted to number of moles of O_2 released into the headspace using the ideal gas law. Since both sensors are time-aligned, at each instant, both gas phase and electrolyte phase O_2 amount (moles) is added to produce the total number of moles of O_2 present in the cell at any instant. Subsequently, the total number of moles of O_2 is converted into equivalent anodic charge by considering that $4e^-$ are released per mole of O_2 produced. The subtraction of OER charge from the total anodic charge emanating from the potentiostat dissolution charge was inferred by subtracting the oxygen charge from the total electric charge (measured by the potentiostat). While the oxygen was continuously monitored in real-time throughout the electrochemical sequence, the oxygen reduction reaction charge at the OCP, which corresponds to the oxygen reduction reaction, was subtracted from the data, since we are only interested in the anodic reaction OER in the transpassive regime. All the above-mentioned steps were automated using a Python script.

2.8 Electron backscattered diffraction measurements and analysis of grain boundary nature

The grain structures and GBCDs of all the three alloys were characterized using EBSD in a Helios NanoLab 600i DualBeam SEM equipped with an Oxford Symmetry detector, all imaging was carried out with 20 kV accelerating voltage, a step size of 0.75 μm was used for Alloy 600 and model alloy recrystallized at 850ºC while it was 1.5 μm for Alloy 800 and model alloy recrystallized at 1100 ºC, and pixels with mean angular deviation > 0.8 were filtered out. The analysis of the EBSD data was carried out using an open-source analysis code based on MATLAB – MTEX [39].

We use CSL theory to classify GBs and identify special GBs based on CSL numbers (Σn). In general, the literature classifies following GBs or class of GBs as special, they are (i) Σ3 (the annealing twin boundary), (ii) $\Sigma 3^n$ boundaries, and (iii) low-CSL GBs with $\Sigma \leq 29$. We quantify and report all the three classes to make sure not to miss any correlation. However, the quantification itself is subjective, and the amount depends on the angular tolerance used to classify a GB as particular CSL. While a particular CSL GB has a theoretical misorientation angle, boundary plane and direction defined, there is an acceptable angular deviation from the theoretical misorientation angle for the boundary to still be considered as a CSL GB. There are several criteria used for angular deviation. Brandon's criterion [40] (Eq. 5) is the most widely used criterion, even though it allows for larger spread. Another competing criterion was proposed by Palumbo and Aust[30], this is based on the ability of the GB to exhibit special properties corresponding to a CSL GB, and it is more restrictive as can be seen from the Eq. 6. Furthermore, the choice of 15^o as pre-factor is rather arbitrary based on low-angle to high-angle GB transition. Thomson and Randle [41] suggested that one could further refine definition of a "perfect" CSL, by considering a lower pre-factor (5^o) – Eq. 7, 8. Depending on the criteria used, fraction of GBs classified to a particular CSL boundary would change, this leads to an uncertainty in quantification of special CSL GB fraction from EBSD data. The error bars reported in Figures 5e and 6e are representative of this spread.

$$\Delta\theta_{Brandon} = 15^o(\Sigma)^{-\frac{1}{2}} \quad (5)$$

$$\Delta\theta_{Palumbo-Aust} = 15^o(\Sigma)^{-\frac{5}{6}} \quad (6)$$

$$\Delta\theta_{Brandon,perfect} = 5^o(\Sigma)^{-\frac{1}{2}} \quad (7)$$

$$\Delta\theta_{Palumbo-Aust,perfect} = 5^o(\Sigma)^{-\frac{5}{6}} \quad (8)$$

3. Results and Discussion

3.1 in situ Respirometry and OER-Dissolution interplay in Ni-Cr-Fe alloys

The charge density vs. time plot for Alloy 600 (Figure 2a), from a representative potentiodynamic-respirometry experiment shows that no oxygen evolved up to +2 $V_{Ag/AgCl}$ and the entire anodic charge was due to the dissolution of the alloy. The cumulative dissolution charge density in the representative experiment was +380 $C.cm^{-2}$ and Cr (III) oxidation likely contributes the most to the overall alloy dissolution, since the onset potential of transpassive

dissolution in Alloy 600 (~0.5 V_{SCE}), is close to that of Cr +0.4 V_{SCE} [5]. Furthermore, the presence of Cr(VI) in the solution was corroborated using the characteristic yellow coloration of the electrolyte. Previously, Oblonsky and Ryan reported based on in situ X-ray absorption near-edge spectroscopy [42], that Ni cannot prevent Cr from further oxidation in binary Ni-18Cr alloy in an acidic sulfate environment and the alloy behaved like pure Cr, consistent with our observations. Conversely, the charge density vs. time plot for Alloy 800 (Figure 2b) presents a contrasting picture with 45% of cumulative anodic charge density going to water oxidation with the rest going to dissolution. Interestingly, the cumulative alloy dissolution charge density was only 60 $C.cm^{-2}$, dropping by a remarkable amount in comparison to Alloy 600.

The inhibition of dissolution in Alloy 800 may be attributed to the effect of Fe (Alloy 800 has 44.29 wt.% Fe compared to 8.53wt.% in Alloy 600). The beneficial effect of Fe has been attributed to secondary passive layer comprising of Fe(III) likely in the form of Fe-rich Ni(Fe)OOH [43], which prevents Cr(III) to Cr(VI) oxidation [44], when Fe ≥ 10 wt.% [45]. The transpassive film formed at pH =5 sulfate on Ni was found to have signature of γ phase of NiOOH with a layered, rhombohedral structure[46]; it is expected that Ni(Fe)OOH could also have a similar structure, but further studies are necessary to ascertain crystallinity as well as the structure.

The Fe-doped NiOOH film is a known OER catalyst in the electrocatalysis literature[47], explaining the significant OER current in Alloy 800 due to strong likelihood of Fe incorporation in the NiOOH. However, one could argue that even the undoped NiOOH, such as the one formed on pure Ni, should catalyze OER to a considerable extent. It is more pertinent since the catalytic nature of NiOOH secondary passive film on pure Ni has been shown in our recent series of papers [18, 37, 38]. However, such an argument is not tenable for Cr-passivated low Fe alloy like the Alloy 600. In Alloy 600, Ni being a relatively noble element in the alloy cannot compete with Cr(III)/Cr(VI) oxidation to form the NiOOH film at least until Cr is considerably depleted in the surface by selective leaching. The Fe content of Alloy 600 further makes the formation of Ni,Fe-based secondary passive film difficult, the 8.43 wt.%Fe in Alloy 600 is less than the 10 wt.% threshold required for secondary passivity as shown by Zhang et al.[45], and consequently,

Fe cannot curb Cr(III)/Cr(VI) oxidation to allow Ni the possibility to form NiOOH film in the first place.

There is an intrinsic difficulty to use *ex situ* techniques to characterize the secondary passive film composed of NiOOH, in absence of an applied external potential control, due to the transient nature of Ni (III) when potential control is removed. In our recent study on pure Ni in the same electrolyte[37] we showed that the NiOOH transpassive film lost its stability immediately upon releasing the potential control (i.e. the film reduces back to Ni (II) upon returning to OCP), based on operando Raman measurements. Furthermore, there are several studies to be found in the literature that rule out characterization of Ni(III)-based secondary passive film using *ex situ* surface analytical techniques such as XPS or UV photoelectron spectroscopy [48, 49].

Nevertheless, ex situ XPS is useful to show that Fe was incorporated into the transpassive film only in the case of high-Fe (~41 wt.%) containing Alloy 800 and was absent in low-Fe containing (~8 wt.%) Alloy 600. Therefore, the next subsection presents the evidence from *ex situ* XPS to bolster the claims of Fe affecting the transpassive film nature.

3.2 Ex-situ XPS analysis

Ex-situ XPS performed post-transpassive polarization on the two commercial alloys (Alloy 600 and Alloy 800), clearly demonstrates that Fe was oxidized and incorporated into the transpassive film of Alloy 800, while Fe was absent in the film as well as at the film/alloy interface in Alloy 600. In Alloy 800, Fe 2p spectrum (Figure 3a) shows a clear metallic Fe peak as well as oxidized Fe peak corresponding to the 2p3/2 level binding energy (BE). The $Fe_{oxidized}$ $2p_{3/2}$ peak in Figure 3a is likely a combination of Fe(II) and Fe(III) species, with predominant Fe(III). The $2p_{1/2}$ level BE window is noisy due to poor signal-to-noise ratio, and no further inference is drawn to avoid overinterpretation. Moreover, $2p_{1/2}$ level peaks are weaker than $2p_{3/2}$ with their expected integrated intensity (area) in the ratio of 1:2[50-52]. Therefore, the noisy spectrum in $2p_{1/2}$ level BE window does not invalidate the claim that Fe is oxidized and incorporated into the film. Ni $2p_{3/2}$ spectrum on the same alloy shows a strong metallic Ni peak with a minor Ni(II) species peak, shake-up satellites are not discernible, consistent with limited Ni oxidation. Cr 2p spectrum from Alloy 800 shows peaks of metallic Cr and Cr(III) species in both $2p_{1/2}$ and $2p_{3/2}$ level BE windows. The 1:2 integrated intensity ratio between $2p_{1/2}$ and $2p_{3/2}$ is evident in the Cr 2p spectrum.

On the other hand, in Alloy 600, Fe is neither present in the oxidized film nor present significantly at the alloy/film interface as seen in Figure 3b. In the region where Fe 2p peak is expected, we observe only a shifting background (see y-axis range) with a broad hump around 708-710 eV, likely corresponding to Ni $L_3M_{23}M_{45}$ Auger signal present in this range. When Fe is significantly present and oxidized, the Ni $L_3M_{23}M_{45}$ Auger line is buried inside the Fe 2p spectrum and shows up clearly only in absence of Fe. The Ni $2p_{3/2}$ spectrum in Alloy 600 shows a stronger Ni (II) peak with a smaller metallic Ni peak, the shake-up satellite also becomes discernible, consistent with increased Ni oxidation in this alloy. Cr 2p spectrum does not show any significant difference from that of Alloy 800. A summary of peak positions used in the above interpretation as well as the corresponding references are listed in Table 2.

The ex-situ XPS analysis is presented solely to clarify that Fe is incorporated into the transpassive film in Alloy 800, while it is not in Alloy 600. The exact nature of the transpassive film cannot be determined using ex-situ XPS, as Ni(III) in the Ni(Fe)OOH is a transient species in the acidic environment and it reduces back to Ni(II) in the absence of external potential control, as discussed earlier, consistent with the observation of only the Ni(II) species in the XPS spectra presented above.

3.3 Transpassive IGC and the role of grain structure

Beyond general material loss, it is important to investigate the attack morphology, as localized corrosion is more detrimental to structural integrity. Figure 4 presents a comparison between the attack morphology of both alloys after the corrosion test. Alloy 600 suffered severe intergranular attack and extensive grain fall-out (Figure 4 b,d) while the Alloy 800 also suffered from IGC in the form of ditching, with sparing grain-fallout. Figure 5a shows 3D confocal laser images and 5b shows the depth of attack probability density plot showing the probability density for both the alloys. It is clear that there is a significant difference between the depth of attack for both alloys. In low-Fe containing Alloy 600, the average and maximum depths of GB attack were 21.2 ± 4.9 μm, and 34.7 μm, respectively. On the other hand, for Alloy 800, the average and maximum depths of GB attack were 7.92 ± 3.64 μm, and 19.8 μm. Therefore, Alloy 800 not only outperformed Alloy 600 in terms of general corrosion resistance but also in localized corrosion.

The improved resistance to transpassive IGC in Alloy 800 as compared to Alloy 600 cannot be purely explained based on alloy chemistry and requires microstructural considerations. We hypothesize that it is related to the GB character distribution as it occurs in absence of Cr depletion. One may contest that there is a distinct possibility of carbide precipitation, and Cr-depletion even in the unsensitized condition. However, in the present case this cannot be the reason for the different susceptibility to IGC, as Cr-depletion (if present) at the GB is incapable of triggering IGC in the transpassive regime. Because the classical form of IGC occurs in the passive conditions, where the alloys derive their passivity from an adequate presence of Cr (Cr_2O_3-enriched passive film), and Cr-depletion at the GBs make them susceptible to IGC. However, Cr is no longer the protective passivating element in the transpassive regime but rather a detrimental agent promoting accelerated dissolution [4, 17], as shown and discussed earlier. As Cr promotes the dissolution in the transpassive regime, its depletion at the GBs could have slowed down dissolution at GBs, contradicting the observation of IGC. Consequently, possible Cr depletion cannot explain the attack seen in Figure 4.

Before proceeding to analyze the relationship between special boundaries and the transpassive IGC, it is essential to establish that there is no statistically meaningful difference in the grain sizes of the alloys that may also impact IGC. Figure 6 shows the EBSD IPF-maps for Alloy 600 (Figure 6a), Alloy 800 (Figure 6b), and the probability density vs. grain diameter for both alloys (Figure 6c). It is clearly seen that there is not a considerable difference between the grain sizes, in the context of their impact on corrosion resistance, as it usually require grain sizes to differ by order(s) of magnitude [53]. When we compare the average grain size, it only differed by ~5 μm (27 μm in Alloy 800 vs. 32 μm in Alloy 600), which further shows that the grain size of both alloys was practically the same.

Figure 7a,b shows the special coincidence-site lattice (CSL) boundaries ($\Sigma \leq 29$) marked over the band-contrast map on Alloy 600 and Alloy 800, respectively. It is evident that Alloy 800 has the higher number density of special boundaries in comparison to Alloy 600. Moreover, as noted earlier, it has been reported that it is not just the number density of special CSL boundaries, but special GB triple junctions, with at least 2 intersecting CSL boundaries (referred to as J2 junctions) that influences the IGC [31-34]. J2 junctions prevent the percolation of IGC, since an attack front cannot advance at a triple junction, with two resistant boundaries. Therefore, Figure 7c,d shows J2 triple junctions overlaid over the IPF map for Alloy 600 and Alloy 800,

respectively. It is again clear that the number density of J2 in Alloy 800 is higher than Alloy 600. It should be noted that for the triple junction analysis, we used only the Σ3 boundaries. However, as shown by several studies, the trends in Σ3 boundaries hold for all low-Σ CSL boundaries[54, 55] .

While Figures 7a-d showed qualitatively higher number density of CSL boundaries and J2 junctions, since the maps were taken over different areas, it is necessary to compare their relative fractions. The CSL boundaries were normalized to the total length of GB segments, while J2 was normalized to total number of junctions. The data is summarized in Figure 7e, the error bars represent the uncertainty in CSL classification from different angular tolerance criteria [30, 40, 41](as described in section 2.7). The histograms are consistent with the visual interpretation from Figure 5a-d, that Alloy 800 possessed structural features that make them resistant to IGC.

From the above discussion, the ability of the Alloy 800 to resist grain-fallout (Figure 4e,f) shows an evident correlation with the higher content of low-Σ CSL boundaries and resistant GB triple junctions than in the Alloy 600. Since both alloys were fully annealed, the origin of variation of special boundary fraction must be analyzed in the context of differences in alloy chemistries between the two alloys. It is an established fact that lower stacking fault energies (SFE) promote higher Σ3 boundary fraction, which is the most prevalent CSL GB for the alloys under consideration. Considering the role of different alloying elements, Fe additions lower the SFE of ternary Ni-Cr-Fe alloys [56, 57]. From the data reported by Arora and Aidhy, at a fixed Cr content = 20 at.%, an increase of Fe from 10 at.% to 40 at.% lowers the SFE from ~80 mJ/m^2 to ~30 mJ/m^2 [56]. We can apply this to Alloy 800 (with ~40% Fe), where the higher Σ3 content can be explained by a lowered SFE. However, since the exact thermomechanical histories of Alloy 600 and Alloy 800 are not known beyond annealing, Fe addition driving increased special CSL boundaries and J2 junctions in commercial alloys must be treated as a hypothesis with correlation, not as causation. Because thermal history prior to annealing is known to significantly alter special boundary formation[58]. Future work changing Fe content with tight control of thermomechanical history would bring further clarity. Moreover, the Cr content differs slightly between in Alloy 800 and Alloy 600, which could influence the SFE. However, we cannot attribute the increased fraction of Σ3 in Alloy 800 to Cr as the effect of Cr is influenced heavily

by its local coordination in the alloy lattice and can even lead to increased SFE under certain conditions, as discussed elsewhere [57].

3.4 Decoupling Fe alloying effect from microstructure effect

As Fe alloying and special GB effects are not decoupled, model Ni-15Cr-10 Fe alloy recrystallized at two temperatures (850^{o} C for 1 h, and 1100^{o} C for 30 min) were tested under same electrochemical conditions. The electrochemical-respirometric plot in Figure 8a,b reveals that the overall dissolution kinetics as well as OER kinetics was insensitive to recrystallization temperature and the resultant microstructure. Unlike Alloy 600, the model alloy with 10Fe showed considerable OER, this can be rationalized through the Fe content of the model alloy meeting the secondary passivity threshold of 10 wt.% [45]. This clearly shows that OER-dissolution interplay is largely governed by Fe content exceeding a threshold for secondary passive film formation and curbing of Cr(III)/Cr(VI) oxidation, irrespective of grain size, grain structure, or their interconnectivity.

The attack morphology in Figure 8c,d shows that the alloy recrystallized at 850^{o} C underwent limited IGC than the alloy recrystallized alloy at 1100^{o} C (deeper IGC). Figure 8e summarizes the statistics of special GBs and J2 junctions (corresponding EBSD-IPF map and CSL overlay can be found in Figure S1 in supplementary materials), the IGC resistance do not correlate positively with the special GB fraction, but it clearly increases with increasing J2 fraction. Therefore, transpassive IGC resistance improves with increasing special GB interconnectivity than the mere increase in special GB fraction.

3.5 Other confounding factors affecting differences in IGC susceptibility

However, one must be aware of other confounding factors while interpreting the results. The impurity contents (e.g. P, S, B) are considerably higher in the commercial alloys than in the model alloy (Table 1), whose segregation could exacerbate IGC. The impurity effect is evident by comparing Figure 4 and Figure 8c,d that the severity of IGC is invariably higher in the commercial alloys than the model alloy.

It is noteworthy that previous studies reporting the beneficial influence of special CSL boundaries on classical IGC attributed either to its ability to resist carbide precipitation [34], and/or increased capability to heal Cr depletion [59]. However, potentially new perspective from

this work is that even without the possible effects of special GBs on precipitation or microchemistry, these may be intrinsically more resistant to attack than a random GB. It must be emphasized that the interconnectivity of special GBs is important to resist transpassive IGC. Therefore, during alloy development, we must not only attempt to increase the special GB fraction but ensure that their interconnectivity is enhanced, to avoid situations such as in the model alloy.

Limitations

The main intention of the paper is to investigate alloy chemistry and microstructural effects on transpassive corrosion mechanisms in Alloy 600 and Alloy 800; therefore, electrolyte composition was fixed at 0.1M K_2SO_4. However, it is likely that anions in the electrolyte could have an effect on the OER-dissolution interplay. Therefore, future studies could explore the role of electrolyte composition on this behavior, at a fixed alloy composition

Conclusions

In this study, we investigated transpassive corrosion of non-sensitized Ni-Cr-Fe alloys probing metallurgical factors governing the interplay between oxygen evolution reaction (OER) on the surface and transpassive dissolution of the alloy itself as well as the localized intergranular corrosion (IGC). The study utilized two commercial alloys, namely Alloy 600 and Alloy 800 along with an arc melted model Ni-15Cr-10Fe alloy in fully annealed condition to accomplish its intended goals. The study used a combination of electrochemical polarization coupled with *in situ* respirometry and ex situ XPS analysis to probe the OER-transpassive dissolution interplay, while it used advanced grain structure characterization using EBSD together with post-mortem corrosion morphology characterization and 3D laser scanning microscopy to study the IGC behavior. Following main conclusions can be drawn from the results:

- The interplay of OER and transpassive dissolution is governed predominantly by the Fe content, especially the Fe content exceeding a seeming critical threshold of 10 wt.% and seems to be insensitive changes in grain structure. OER seems to contribute to almost 50% of anodic charge when Fe content exceeds the threshold as seen in Alloy 800 and the model alloy.

- The transpassive IGC seems to be influenced by both Fe content as well as grain boundary character distribution and interconnectivity of the special CSL GBs, but the predominantly latter because it was shown that it is possible to mitigate transpassive IGC in a low Fe containing model alloy by tuning special GBs and triple junctions via thermomechanical treatment. Even in the case of commercial alloys, Fe content effect on transpassive IGC was likely through its influence on special GBs through lowering of SFE.

Acknowledgements

The authors thank Ms. Ann-Kathrin Bach for assistance with some of the respirometry measurements. The authors thank Mr. Felix Feyer for their assistance with the spark OES measurements. KH and KK acknowledge useful discussions with Sudharsan Sundar (Chimie ParisTech, France) on interpretation of XPS spectra. KH thanks useful technical discussions with Prof. V.S. Raja, Prof. Indradev Samajdar, Prof. Philippe Marcus, and Dr. Narasi Sridhar.

Funding statement

Funding by the Deutsche Forschungsgemeinschaft (DFG, German Research Foundation) Project-ID 517690381 (VI 350/13–1) is acknowledged. (KH, KK and SV)

KH acknowledges the financial support of the Alexander von Humboldt foundation through Humboldt postdoctoral fellowship.

CreDiT contribution statement

Karthikeyan Hariharan: Conceptualization, Methodology, Writing – Original draft, Visualization, Supervision, Fund acquisition. **Koushik Kosanam:** Investigation, Methodology, Formal Analysis, Writing – review and editing. **Elisabeth Kammermeir**: Investigation, Writing – review and editing. **Christopher H. Zenk**: Writing – review and editing, Supervision, Resources. **Sannakaisa Virtanen:** Conceptualization, Supervision, Fund acquisition, Writing – review and editing.

Data availability

The data supporting this work will be made available on request.

Declaration of competing interests

Authors declare no known competing interests that may affect the findings of this study

References

[1] P. Schmuki, From Bacon to barriers: a review on the passivity of metals and alloys, Journal of Solid State Electrochemistry, 6 (2002) 145-164.
[2] M. Bojinov, G. Fabricius, P. Kinnunen, T. Laitinen, K. Mäkelä, T. Saario, G. Sundholm, The mechanism of transpassive dissolution of Ni–Cr alloys in sulphate solutions, Electrochimica Acta, 45 (2000) 2791-2802.
[3] A.W.E. Hodgson, S. Kurz, S. Virtanen, V. Fervel, C.O.A. Olsson, S. Mischler, Passive and transpassive behaviour of CoCrMo in simulated biological solutions, Electrochimica Acta, 49 (2004) 2167-2178.
[4] P.T. Wilson, N.J. Laycock, M.P. Ryan, D.S. Crouch, H.S. Isaacs, Transpassive Corrosion of Stainless Steels and Nickel-Base Alloys, in: CAP, Auckland, NZ, 2000.
[5] P. Schmuki, S. Virtanen, A.J. Davenport, C.M. Vitus, Transpassive Dissolution of Cr and Sputter-Deposited Cr Oxides Studied by In Situ X-Ray Near-Edge Spectroscopy, Journal of The Electrochemical Society, 143 (1996) 3997.
[6] L.H. Prado, S. Virtanen, N. Weineck, A. Ghicov, F. Kessler, How to perform corrosion experiments for proton exchange membrane water electrolysis bipolar plates, Journal of Power Sources, 613 (2024) 234815.
[7] G. Liu, F. Hou, S. Peng, X. Wang, B. Fang, Process and challenges of stainless steel based bipolar plates for proton exchange membrane fuel cells, International Journal of Minerals, Metallurgy and Materials, 29 (2022) 1099-1119.
[8] M. Dadfar, M. Salehi, M. Golozar, S. Trasatti, M. Casaletto, Surface and corrosion properties of modified passive layer on 304 stainless steel as bipolar plates for PEMFCs, international journal of hydrogen energy, 42 (2017) 25869-25876.
[9] X. Li, P. Zhou, K. Ogle, S. Proch, M. Paliwal, A. Jansson, J. Westlinder, Transient stainless-steel dissolution and its consequences on ex-situ bipolar plate testing procedures, International Journal of Hydrogen Energy, 45 (2020) 984-995.
[10] A. Maki, Corrosion circumstance in the Tokai Reprocessing Plant and evaluation of the corrosion rate, Saikuru Kiko Giho, (2002) 39-63.
[11] D.N.T. Barton, T. Grebennikova, A.E. Denman, T. Carey, D.L. Engelberg, C.A. Sharrad, Long-term aqueous contamination of stainless steel in simulant nuclear reprocessing environments, Journal of Nuclear Materials, 583 (2023) 154551.
[12] P. Fauvet, 19 - Corrosion issues in nuclear fuel reprocessing plants, in: D. Féron (Ed.) Nuclear Corrosion Science and Engineering, Woodhead Publishing, 2012, pp. 679-728.

[13] Z. Szklarska-Smialowska, Z. Xia, R.R. Valbuena, Mechanism of Crack Growth in Alloy 600 in High-Temperature Deaerated Water, Corrosion, 50 (1994) 676-681.
[14] P. Kritzer, N. Boukis, E. Dinjus, Über die transpassive Auflösung von Nickel-Basis-Legierungen und Edelstählen in sauerstoff- und chloridhaltigem Hochtemperatur-Wasser, Materials and Corrosion, 48 (1997) 799-805.
[15] P. Kritzer, N. Boukis, E. Dinjus, Transpassive Dissolution of Alloy 625, Chromium, Nickel, and Molybdenum in High-Temperature Solutions Containing Hydrochloric Acid and Oxygen, Corrosion, 56 (2000) 265-272.
[16] T.P. Moffat, R.M. Latanision, An Electrochemical and X-Ray Photoelectron Spectroscopy Study of the Passive State of Chromium, Journal of The Electrochemical Society, 139 (1992) 1869.
[17] M. Keddam, Anodic dissolution, in: Corrosion mechanisms in theory and practice, CRC Press, 2002, pp. 106-179.
[18] K. Hariharan, A.-K. Bach, M.P. Bruns, S. Virtanen, Transpassive corrosion mechanisms in Ni revisited with electrochemistry coupled in situ respirometry, Electrochimica Acta, (2025) 146461.
[19] M. Strebl, M. Bruns, S. Virtanen, Editors' Choice—Respirometric in Situ Methods for Real-Time Monitoring of Corrosion Rates: Part I. Atmospheric Corrosion, Journal of The Electrochemical Society, 167 (2020) 021510.
[20] M.G. Strebl, M.P. Bruns, G. Schulze, S. Virtanen, Respirometric In Situ Methods for Real-Time Monitoring of Corrosion Rates: Part II. Immersion, Journal of The Electrochemical Society, 168 (2021) 011502.
[21] M.G. Strebl, M.P. Bruns, S. Virtanen, Respirometric in Situ Methods for Real-Time Monitoring of Corrosion Rates: Part III. Deconvolution of Electrochemical Polarization Curves, Journal of The Electrochemical Society, 170 (2023) 061503.
[22] J. Armijo, Intergranular Corrosion of Nonsensitized Austenitic Stainless Steels—1. Environmental Variables, Corrosion, 21 (1965) 235-244.
[23] G. Palumbo, K.T. Aust, Structure-dependence of intergranular corrosion in high purity nickel, Acta Metallurgica et Materialia, 38 (1990) 2343-2352.
[24] G. Economy, R.J. Jacko, F.W. Pement, IGSCC Behavior of Alloy 600 Steam Generator Tubing in Water or Steam Tests Above 360 C, Corrosion, 43 (1987) 727-734.
[25] S.M. Bruemmer, L.A. Chariot, C.H. Henager, Jr., Microstructure and Microdeformation Effects on IGSCC of Alloy 600 Steam Generator Tubing, in: CORROSION 1987, 1987, pp. 1-12.
[26] F. Vaillant, D. Buisine, B. Prieux, Comparative behavior of Alloys 600, 690 and 800 in caustic environments, NACE International, Houston, TX (United States), United States, 1995.
[27] Y.M. Pan, D.S. Dunn, G.A. Cragnolino, N. Sridhar, Grain-boundary chemistry and intergranular corrosion in alloy 825, Metallurgical and Materials Transactions A, 31 (2000) 1163-1173.
[28] A. Anderko, N. Sridhar, G. Tormoen, Localised corrosion of heat-treated alloys Part II – Predicting grain boundary microchemistry and its effect on repassivation potential, Corrosion Engineering, Science and Technology, 45 (2010) 204-223.
[29] P. Lin, G. Palumbo, U. Erb, K.T. Aust, Influence of grain boundary character distribution on sensitization and intergranular corrosion of alloy 600, Scripta Metallurgica et Materialia, 33 (1995) 1387-1392.

[30] G. Palumbo, K.T. Aust, E.M. Lehockey, U. Erb, P. Lin, On a More Restrictive Geometric Criterion for “Special” CSL Grain Boundaries, Scripta Materialia, 38 (1998) 1685-1690.
[31] M. Kumar, W.E. King, A.J. Schwartz, Modifications to the microstructural topology in f.c.c. materials through thermomechanical processing, Acta Materialia, 48 (2000) 2081-2091.
[32] C.A. Schuh, M. Kumar, W.E. King, Analysis of grain boundary networks and their evolution during grain boundary engineering, Acta Materialia, 51 (2003) 687-700.
[33] V.Y. Gertsman, M. Janecek, K. Tangri, Grain boundary ensembles in polycrystals, Acta Materialia, 44 (1996) 2869-2882.
[34] A. Telang, A.S. Gill, D. Tammana, X. Wen, M. Kumar, S. Teysseyre, S.R. Mannava, D. Qian, V.K. Vasudevan, Surface grain boundary engineering of Alloy 600 for improved resistance to stress corrosion cracking, Materials Science and Engineering: A, 648 (2015) 280-288.
[35] S. Choudhary, K. Marusak, T. Eldred, R.G. Kelly, Use of a Bipolar, Metallic Luggin-Haber Probe for Electrochemical Measurements of Interfacial Potential, Journal of The Electrochemical Society, 169 (2022) 111505.
[36] C. Xie, J. Yuan, K. Hariharan, S. Virtanen, J. Han, K. Ogle, Integrating AESEC with the Respirometric method: A New Approach to Unraveling OER and Dissolution Phenomena, Electrochimica Acta, 556 (2026) 148319.
[37] K. Hariharan, K. Kosanam, C. Götz, M.P. Bruns, T. Böhm, P. Marcus, N. Sridhar, S. Virtanen, On the Proposed Mechanism of Transpassive Film Formation in Pure Ni in Sulfate Environment: Insights from In Situ Raman Spectroscopy and Respirometry, Journal of The Electrochemical Society, 173 (2026) 031501.
[38] C. Xie, J. Yuan, K. Hariharan, S. Virtanen, J. Han, K. Ogle, Integrating AESEC with the Respirometric method: A New Approach to Unraveling OER and Dissolution Phenomena, Electrochimica Acta, (2026) 148319.
[39] F. Bachmann, R. Hielscher, H. Schaeben, Texture Analysis with MTEX – Free and Open Source Software Toolbox, Solid State Phenomena, 160 (2010) 63-68.
[40] D.G. Brandon, The structure of high-angle grain boundaries, Acta Metallurgica, 14 (1966) 1479-1484.
[41] C.B. Thomson, V. Randle, “Fine tuning” at Σ3n boundaries in nickel, Acta Materialia, 45 (1997) 4909-4916.
[42] L.J. Oblonsky, M.P. Ryan, In Situ X-Ray Absorption Near-Edge Structure Study of the Active and Transpassive Dissolution of Passive Films on Ni and Ni-Cr Alloys in 0.1 M H_2SO_4, Journal of The Electrochemical Society, 148 (2001) B405.
[43] P. Guo, X. Lin, D.D. Macdonald, B. Ter-Ovanessian, J. Liu, G. Song, Y. Zhang, Y. Ren, H. Lan, W. Huang, Unveiling the transpassive film failure of 3D printing transition alloys, Corrosion Science, 204 (2022) 110412.
[44] E.J. Calvo, C.D. Pallotta, S. Hild, E. Garcia, XPS and Electrochemical Studies of Chromium Modified Passive Iron Electrodes, Journal of The Electrochemical Society, 135 (1988) 314.
[45] Z. Zhang, B. Ter-Ovanessian, S. Marcelin, J. Galipaud, B. Normand, Role of Alloying Elements in Passive and Transpassive Behavior of Ni–Cr-Based Alloys in Borate Buffer Solution, Journal of The Electrochemical Society, 168 (2021) 081503.

[46] γ-NiOOH (NiO[OH] rhom) Crystal Structure: Datasheet from "PAULING FILE Multinaries Edition – 2022" in SpringerMaterials (https://materials.springer.com/isp/crystallographic/docs/sd_1703913), in: P. Villars, K. Cenzual (Eds.), Springer-Verlag Berlin Heidelberg & Material Phases Data System (MPDS), Switzerland & National Institute for Materials Science (NIMS), Japan.
[47] Z. Lin, P. Bu, Y. Xiao, Q. Gao, P. Diao, β- and γ-NiFeOOH electrocatalysts for an efficient oxygen evolution reaction: an electrochemical activation energy aspect, Journal of Materials Chemistry A, 10 (2022) 20847-20855.
[48] H.-W. Hoppe, H.-H. Strehblow, XPS and UPS examinations of passive layers on Ni and FE53Ni alloys, Corrosion Science, 31 (1990) 167-177.
[49] J. Gallenberger, H.M. Fernández, A. Alkemper, M. Li, C. Tian, B. Kaiser, J.P. Hofmann, Stability and decomposition pathways of the NiOOH OER active phase of NiO x electrocatalysts at open circuit potential traced by ex situ and in situ spectroscopies, Catalysis Science & Technology, 13 (2023) 4693-4700.
[50] L. Wang, S. Zanna, D. Mercier, V. Maurice, P. Marcus, Early-stage surface oxidation of the equiatomic CoCrFeMnNi high entropy alloy studied in situ by XPS, Corrosion Science, 220 (2023) 111310.
[51] A.E. Hughes, C.D. Easton, T.R. Gengenbach, M.C. Biesinger, M. Laleh, Interpretation of complex x-ray photoelectron peak shapes. II. Case study of Fe 2p3/2 fitting applied to austenitic stainless steels 316 and 304, Journal of Vacuum Science & Technology A, 42 (2024).
[52] M.C. Biesinger, B.P. Payne, A.P. Grosvenor, L.W.M. Lau, A.R. Gerson, R.S.C. Smart, Resolving surface chemical states in XPS analysis of first row transition metals, oxides and hydroxides: Cr, Mn, Fe, Co and Ni, Applied Surface Science, 257 (2011) 2717-2730.
[53] K.D. Ralston, N. Birbilis, Effect of Grain Size on Corrosion: A Review, Corrosion, 66 (2010) 075005-075005-075013.
[54] M. Bettayeb, V. Maurice, L.H. Klein, L. Lapeire, K. Verbeken, P. Marcus, Nanoscale Intergranular Corrosion and Relation with Grain Boundary Character as Studied In Situ on Copper, Journal of The Electrochemical Society, 165 (2018) C835.
[55] Y.Q. Zhang, G.Z. Quan, J. Zhao, Y.Z. Yu, W. Xiong, A Review on Controlling Grain Boundary Character Distribution during Twinning-Related Grain Boundary Engineering of Face-Centered Cubic Materials, Materials (Basel), 16 (2023).
[56] G. Arora, D.S. Aidhy, Machine Learning Enabled Prediction of Stacking Fault Energies in Concentrated Alloys, Metals, 10 (2020) 1072.
[57] J. Fischer, D.S. Aidhy, Local charge distortion due to Cr in Ni-based concentrated alloys, Acta Materialia, 279 (2024) 120285.
[58] D.L. Engelberg, R.C. Newman, T.J. Marrow, Effect of thermomechanical process history on grain boundary control in an austenitic stainless steel, Scripta Materialia, 59 (2008) 554-557.
[59] D. Wasnik, V. Kain, I. Samajdar, B. Verlinden, P. De, Resistance to sensitization and intergranular corrosion through extreme randomization of grain boundaries, Acta Materialia, 50 (2002) 4587-4601.
[60] S.X. Chen, Probability density function estimation using gamma kernels, Annals of the institute of statistical mathematics, 52 (2000) 471-480.

[61] L. Ma, F. Wiame, X. Chen, X. Ma, Effect of Nb on the surface composition of FeCrAl alloys after anodic polarization, Materials & Design, 219 (2022) 110728.
[62] B. Lynch, F. Wiame, V. Maurice, P. Marcus, XPS study of oxide nucleation and growth mechanisms on a model FeCrNiMo stainless steel surface, Applied Surface Science, 575 (2022) 151681.
[63] R. Allenspach, D. Mauri, M. Taborelli, M. Landolt, Spin-polarized Auger-electron spectroscopy, Physical Review B, 35 (1987) 4801-4809.

Figures and Figure Captions

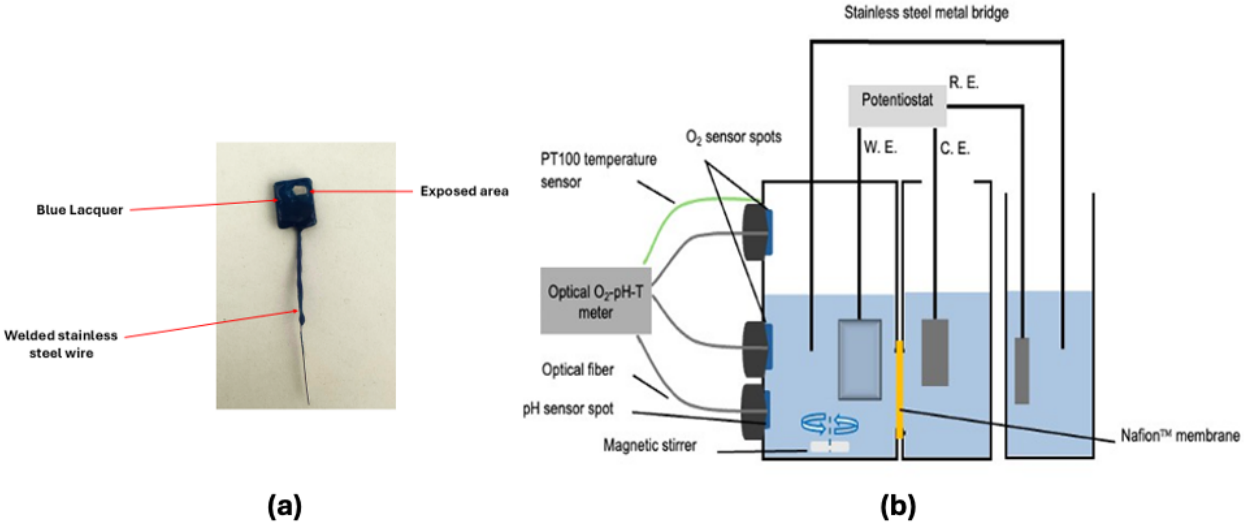

Figure 1 – (a) The specimen used for potentiodynamic-respirometry experiment along with blue laquear coating and the spot welded 304L stainless steel wire, **(b)** Schematic drawing of the potentiodynamic respirometry setup (reproduced with permission from Elsevier based on Ref. 18)

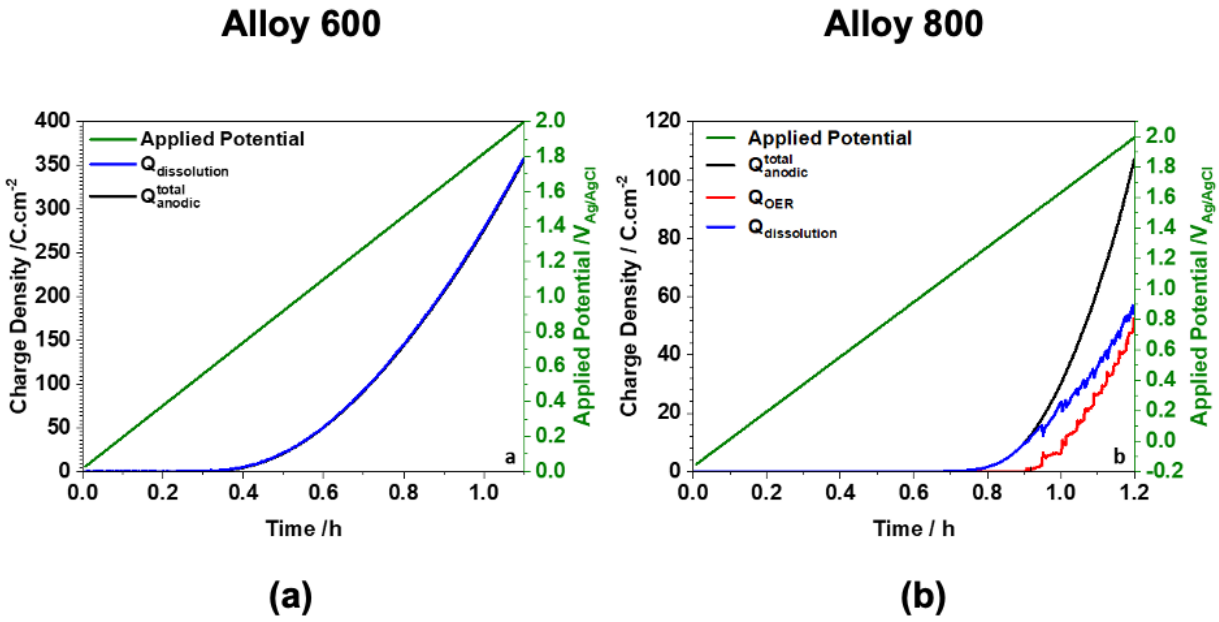

Figure 2 – Charge density vs. time plot during potentiodynamic-respirometry measurements in 0.1 M K_2SO_4 (pH = 5) for (a) Alloy 600 and (b) Alloy 800. Q_{anodic}^{total} represents the total anodic charge measured by the potentiostat, Q_{OER} is the charge associated with the water oxidation reaction, measured through *in situ* respirometry, $Q_{dissolution}$ is the inferred total alloy dissolution charge obtained by subtracting Q_{OER} from Q_{anodic}^{total}.

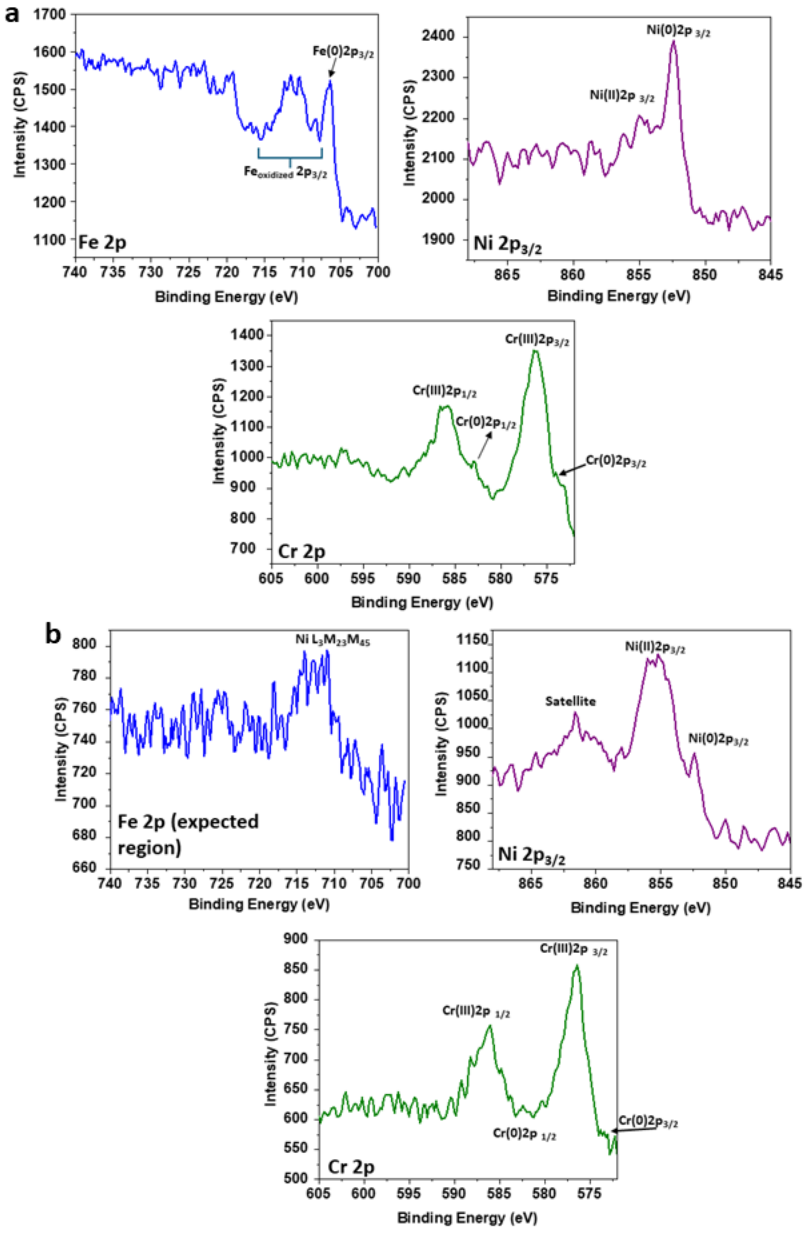

Figure **3**: XPS Fe 2 p, Ni $2p_{3/2}$, and Cr 2p core level spectra for a) Alloy 800 and b) Alloy 600 in after polarization test 0.1M K_2SO_4.

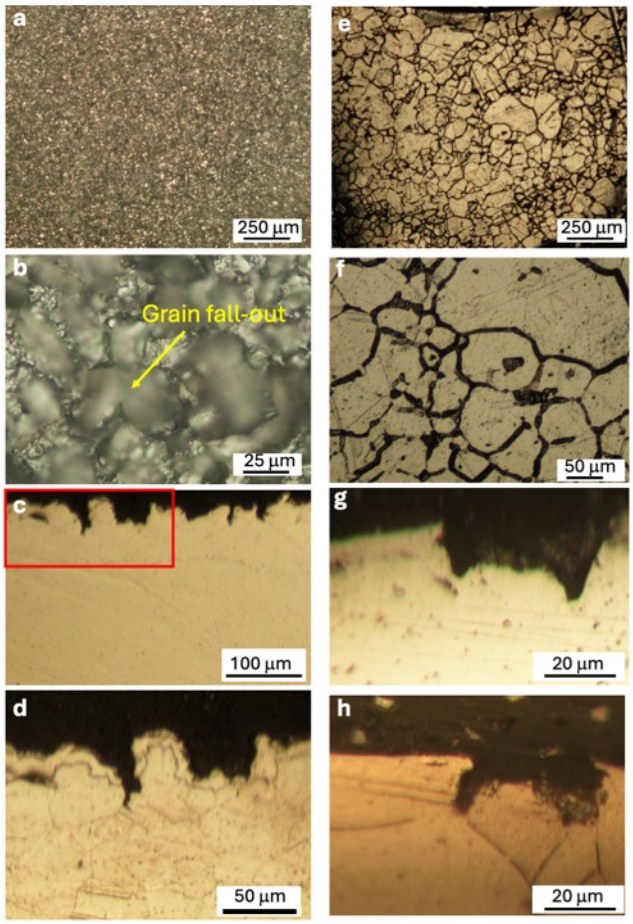

Figure 4 – (a)-(d) Post-mortem optical microscope attack morphology in Alloy 600 – (a) low-magnification top-view, (b) high-magnification top-view indicating grain fallout (yellow arrow), (c) cross-section (unetched) showing the attack front and more evidence of fall-out, (d) cross-section (etched with ASTM etchant No. 25) showing the IGC front – Ni plated layer visible over the front. (e)-(h) Post-mortem optical microscope attack morphology in Alloy 800 - (e) low-magnification top-view, (f) high-magnification top-view showing ditching of GBs (c) cross-section (unetched) showing the attack front and a single event of fallout, (d) cross-section (etched with ASTM etchant No. 25) showing the IGC front

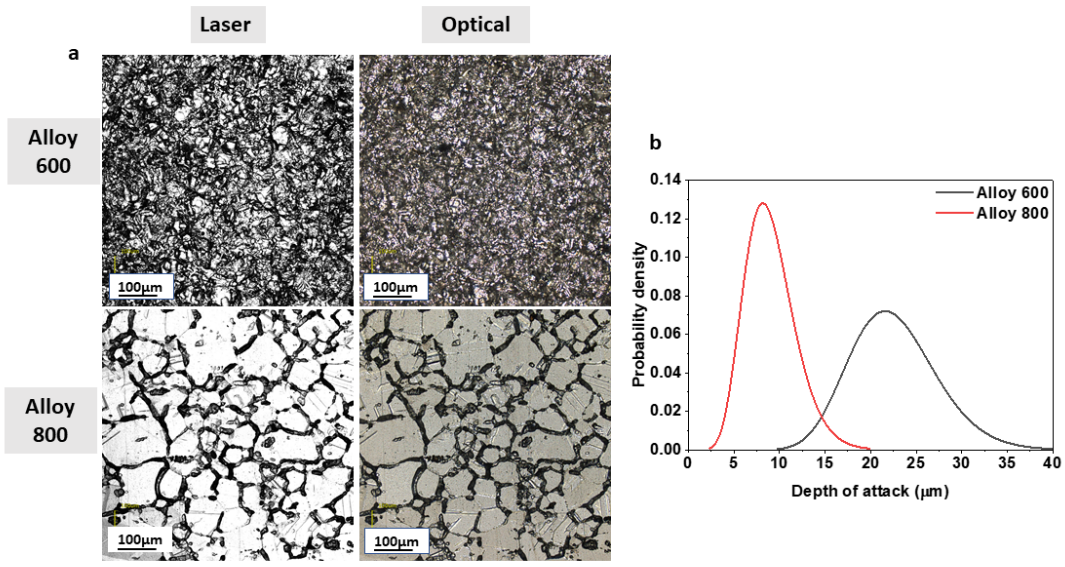

Figure **5**: a) Laser and optical images for alloy 600 and alloy 800 b) Depth of attack probability density plot showing the probability density based on gamma kernel density estimate (GKDE), the choice to use GKDE instead of normal KDE was to correct the boundary bias that led to unphysical negative depth of attack values in the distribution

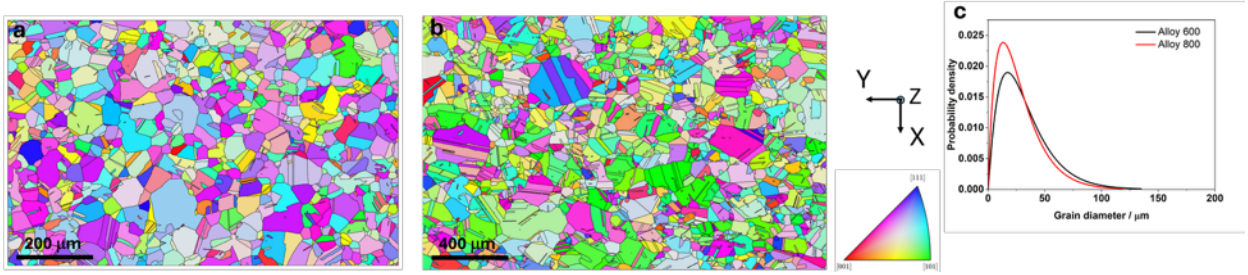

Figure 6 – EBSD-IPF maps for (a) Alloy 600, and (b) Alloy 800. (c) Grain diameter probability density plot showing the probability density based on gamma kernel density estimate (GKDE) [60], the choice to use GKDE instead of normal KDE was to correct the boundary bias that led to unphysical negative grain diameter values in the distribution.

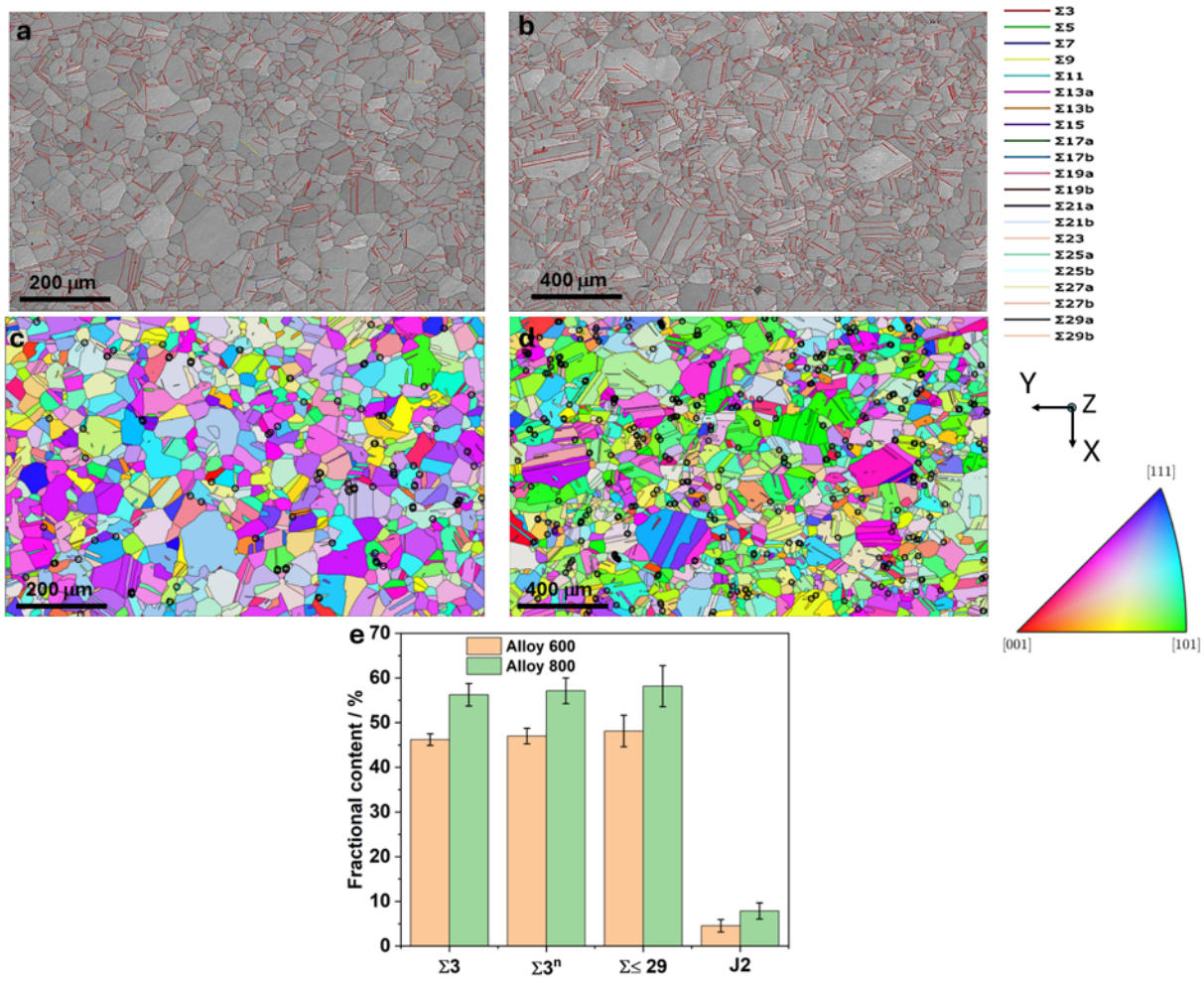

Figure 7 – CSL boundaries overlaid on EBSD band contrast map for (a) Alloy 600, and (b) Alloy 800. J2 triple junctions marked over EBSD-IPF maps for (c) Alloy 600, and (d) Alloy 800. (e) Statistical summary of $\Sigma 3$, $\Sigma 3^n$, $\Sigma \leq 29$ CSL boundaries and J2 triple junctions in both the alloys.

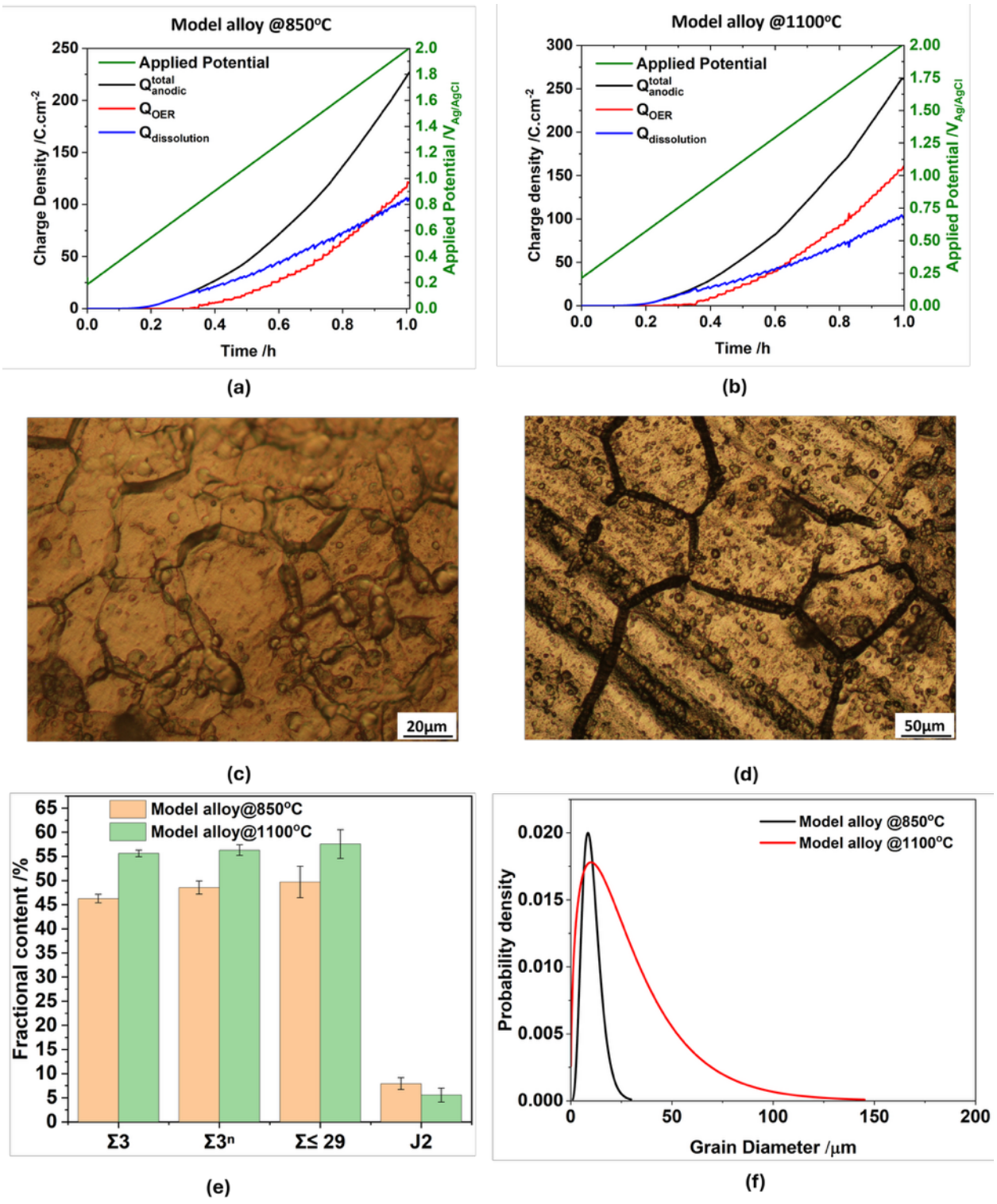

Figure 8 – Charge density vs. time plot during potentiodynamic-respirometry measurements in 0.1 M K_2SO_4 (pH = 5) for model Ni-15Cr-10Fe alloy (a) recrystallized at 850° C for 1 h and (b) recrystallized at 1100° C for 30 min – symbols used as is in Figure 1, (c) corroded surface

showing shallow IGC morphology in 850° C recrystallized model alloy, (d) corroded surface showing deeper IGC morphology in recrystallized 1100° C model alloy, (e) Statistical summary of $\Sigma 3$, $\Sigma 3^n$, $\Sigma \leq 29$ CSL boundaries and J2 triple junctions in model alloys, (f) Grain diameter probability density plot showing the probability density based on gamma kernel density estimate (GKDE) [60].

Table and Table captions

Table 1 – Spark OES measured composition of alloys tested in this study (in wt.%)

Alloy	Cr	Fe	Co	Mn	Nb	W	Mo	Al	Ti	Si	P	C	S	N	Cu	B	Ni
600	16.43	8.53	0.098	0.32	0.085	0.03	0.1	0.18	0.16	0.27	0.013	0.071	0.007	0.034	0.023	0.0004	Bal.
800	19.93	44.29	0.11	0.74	0.21	0.24	0.29	0.4	0.4	0.12	0.017	0.086	0.007	0.054	0.28	0.002	Bal.
Model alloy	15.82	10.08	0.024	-	0.044	0.025	0.061	-	0.008	-	0.006	0.017	0.008	-	-	-	Bal.

Table 2 – XPS spectra peaks and corresponding references

Core level	Chemical state	BE (±0.1eV)	References
Fe $2p_{3/2}$	Fe^0	706.6	[61]
	Fe^{2+}	708.3	[62]
	Fe^{3+}	710.3	[62]
Cr $2p_{3/2}$	Cr^0	573.9	[62]
	Cr^{3+}	576.3	[61]
Cr $2p_{1/2}$	Cr^0	583.2	[61]
	Cr^{3+}	585.8	[61]
Ni $2p_{3/2}$	Ni^0	852.5	[62]
	Ni^{2+}	855	[52]
	Satellite	861.6	[50]
	Ni $L_3M_{23}M_{45}$	1486.6 eV (Al Kα)-779eV = 708 eV (hν-KE=apparent binding energy)	[63]

*KE = Kinetic Energy of Auger signal, hν = the monochromatic incident X-ray energy